Systematic vector solitary waves from their linear limits in one-dimensional n-component Bose-Einstein condensates

Wenlong Wang [*]
College of Physics, Sichuan University, Chengdu 610065, China

(Received 23 December 2020; revised 13 June 2021; accepted 9 July 2021; published 27 July 2021)

We systematically construct a series of vector solitary waves in harmonically trapped one-dimensional three-, four-, and five-component Bose-Einstein condensates. These stationary states are continued in chemical potentials from the analytically tractable low-density linear limit of respective states, as independent linear quantum harmonic oscillator states, to the high-density nonlinear Thomas-Fermi regime. A systematic interpolation procedure is proposed to achieve this sequential continuation via a trajectory in the multidimensional space of the chemical potentials. The Bogoliubov–de Gennes spectral analysis shows that all of the states considered herein can be fully stabilized in suitable chemical potential intervals in the Thomas-Fermi regime. Finally, we present some typical SU(n)-rotation-induced and driving-induced dynamics. This method can be extended to higher dimensions and shows significant promise for finding a wide range of solitary waves ahead.

DOI: 10.1103/PhysRevE.104.014217

I. INTRODUCTION

Solitons are ubiquitous nonlinear excitations in a wide range of dispersive and nonlinear waves, e.g., in Bose-Einstein condensates (BECs) [1,2], and nonlinear optics [3]. In particular, BECs have enjoyed considerable attention over the past decades, providing an ideal playground for investigating (single and multiple) solitonic structures, including studies of their generation, stability, interaction, instability, and associated dynamics and pattern formation [4]. In the single-component one-dimensional setting, bright [5] and dark solitons [6] are arguably the most fundamental structures in attractive and repulsive condensates, respectively. In higher dimensions, novel topological structures bearing vorticity emerge such as vortices [7], vortex rings [8,9], and even knots [10]. Moreover, extended dark solitonic structures, e.g., ring dark solitons in both two and three dimensions [11,12], have also been considered.

In parallel, vector solitons in multicomponent settings are also fascinating. In one-dimensional two-component systems of repulsive interactions, the dark-bright structure has been a central point of theoretical and experimental efforts [13–19]. Here a bright component is trapped (and waveguided) by an effective potential of the dark soliton in the other component. It is important to note that a bright soliton cannot exist on its own in repulsive condensates, i.e., under self-defocusing nonlinearity. More exotic structures such as dark-dark [20,21] and dark-antidark waves [22] have also been found; see, e.g., recent works on magnetic solitons in both binary [23,24] and spinor [25] condensates. Indeed, there has been a flurry of associated activities, as can be attested by recent works [26,27]. These solitary waves may naturally undergo dynamics not accessible in a single-component system [20,28,29]. While the two-component systems have been extensively studied [30,31], there are far fewer studies on systems of three or even more components [25,32]. In this vein, it is especially relevant to highlight the fact that recent experimental studies have rendered accessible a wide range of possibilities, including that of suppressing the effect of spin-dependent interactions [33] and materializing instantiations of the well-known Manakov model originally developed in nonlinear optics [34]. While these recent developments have been predominantly focusing on two- and three-component systems, it is natural to expect that generalizations thereof to $F = 2$ spin systems and up to five-component states are well within reach [35].

There has been tremendous experimental progress on implementing dark soliton winding patterns, and realizing spinor condensates. Dark solitons can be routinely generated using a variety of experimental techniques, enabling an extensive investigation of their collisions and interactions. Multiple dark solitons of varying positions and velocities can be generated using the phase imprinting technique [36–38] using laser pulses. They can also be created using matter-wave interferences [39,40]. Moreover, it is possible to controllably produce dark solitary waves of arbitrary speed [41] in a single component condensate using both density and phase engineering [41–43]. Vector solitary waves can be formed using a spatially dependent spin interconversion and phase imprinting [33,36]. In [33], a spatially localized spin rotation with simultaneous density and phase imprinting was achieved using a steerable laser beam. Spinor condensates can be realized in far detuned optical dipole traps in, e.g., ^{87}Rb spinor condensates [33,44,45] or ^{23}Na spinor condensates [46,47] in the $F = 1$ manifold. An $F = 2$ condensate can be created either directly [48] or alternatively from the $F = 1$ manifold using a microwave excitation [44].

On the theory side, there have been extensive efforts in generalizing the analytical techniques developed for the one-component system to multicomponent systems, e.g., the

---

[*] wenlongcmp@scu.edu.cn

inverse scattering, the Bäcklund transformation, the Darboux transformation, and the Hirota bilinear methods [49–52]. The generalization is, however, frequently not straightforward and often extremely elaborate in its analytical form; see [53] for a modified Darboux transformation and also a relevant discussion. Moreover, these approaches are, by necessity, limited to the (integrable) one-dimensional homogeneous Manakov systems [34] where the intra- and interspecies interactions are equal. This naturally poses the question of developing methods that could be more straightforwardly generalized beyond the integrable realm to provide an understanding of the broad wealth of nonlinear wave states that may become experimentally accessible in this emerging setting of multicomponent BEC systems.

In the nonintegrable setting, e.g., in the presence of a harmonic trap, finding numerically exact stationary states and investigating their near-equilibrium dynamics and dynamical instabilities, if any, are particularly interesting [54]. This is especially true in higher dimensions. The Bogoliubov–de Gennes (BdG) spectra are also natural to compute, encompassing much of the relevant dynamical information through the BdG eigenvalues and eigenvectors. Numerical methods can in principle find stationary solutions in a generic setting. Recently, a deflation method [55–57] was studied which runs iteratively at fixed chemical potentials, and the solver is designed such that a new solution, if converged properly, avoids already found ones by properly modifying the stationary-state equation to solve. This method has found a remarkable series of solutions in both one- and two-component systems. However, the exploration of the solution space is not controlled, and the method inevitably becomes increasingly expensive as more states are added to the list of solutions.

An alternative semianalytical method is to construct solitary waves from the known linear limit in a suitable, e.g., harmonic, potential using the (chemical potential) parametric continuation [58–61]. In the linear limit, the nonlinear term is negligible and the linear problem is fully solvable as different components decouple into independent quantum harmonic oscillators. Perturbation analysis suggests, but does not prove, that a low-density linear state can be continued in chemical potentials to a weakly nonlinear one, and thereafter to a highly nonlinear state in the high-density Thomas-Fermi regime; i.e., a series of solutions can be constructed interpolating the two limits. The spirit of the method is therefore to take advantage of the analytically tractable linear limit by first turning off the nonlinearity and then gradually adding it back. In fact, the recent three-dimensional deflation study also partially employed this idea [57], showing the significance of the method. This method was successfully applied to the one-dimensional two-component system, focusing instead on solitonic beating patterns following a unitary rotation or mixing of the different components, along with two case examples in the three-component setting [61]. It is also worth mentioning that while these states are constructed in the harmonic potential, further continuation to other potentials, e.g., by interpolating between two different potentials is possible, showing the flexibility of the method.

The main purpose of the present work is to systemically construct vector solitary waves from the linear limit for a general n-component system, motivated in particular by the above discussion and the recent experimental implementation of the three-component Manakov model [33]. The availability of $F = 1$ and 2 systems [35] prompts us to illustrate the method for three-, four-, and up to five-component vector solitary waves, and it is likely that these waveforms can be implemented experimentally using the currently available techniques (see Sec. III for a discussion).

An additional motivation is that it is sensible to demonstrate the effectiveness of the method in $1 + 1$ dimensions before further extending it to higher dimensions, where there is a "degenerate state problem" (see Sec. IV). This is worth exploring because there is yet *no a priori* theoretical guarantee that the continuation should be successful and the waveforms can be stabilized. Our approach is so far successful, and a large series of states of increasing complexity are constructed. Despite the expectation that it typically gets increasingly harder to stabilize more complex states, bearing a growing number of the so-called negative energy modes [4], it is remarkable that all of the states considered herein can be properly stabilized in suitable chemical potential intervals as they approach the Thomas-Fermi limit. It should be emphasized that the states constructed herein are genuinely complex, in the sense that a vector solitary wave typically cannot be decomposed into a set of elementary vector solitons such as the dark-dark-bright or dark-bright-bright solitons [62], although such localized structures can be identified in certain spatial regimes. To our best knowledge, the majority of these solitary waves, particularly the highly excited ones bearing multiple phase windings, have not been studied before. The large and organized array of vector solitary waves should provide an excellent platform for studying their detailed properties theoretically and computationally, as well as experimentally.

Finally, some typical dynamics are illustrated. The diverse states should be able to access a rich set of dynamical evolution scenarios, considering also their complexity. Indeed, our direct numerical simulations confirm this expectation. Here, we only present a few prototypical proof-of-principle examples for clarity. Specifically, we focus on two types of dynamics: SU(n)-rotation-induced and driving-induced breathing dynamics. Both periodic and aperiodic evolutions are possible and are illustrated.

The presentation is organized as follows. In Sec. II, we introduce the model, the numerical setup, and the method of constructing vector solitary waves from the linear limit. Next, we present our results in Sec. III. Finally, our conclusions and a number of open problems for future consideration are given in Sec. IV.

II. MODEL AND METHODS

We first present the mean-field Gross-Pitaevskii equation and the SU(n) symmetry for n-component condensates with Manakov interactions, and the numerical methods used for finding stationary states, stability analysis, and dynamics. Then we discuss the method of constructing stationary vector solitary waves from the linear limit using the chemical potential continuation, and the scaling of the number of solitons with the principle or maximum quantum number.

A. Computational setup

In the framework of the lowest-order mean-field theory, and for sufficiently low temperatures, the dynamics of one-dimensional n-component repulsive BECs, confined in a time-independent trap V, is described by the following coupled dimensionless Gross-Pitaevskii equation (GPE) [4,61]:

$$i\frac{\partial\psi_j}{\partial t} = -\frac{1}{2}\psi_{jxx} + V\psi_j + \left(\sum_{k=1}^{n} g_{jk}|\psi_k|^2\right)\psi_j, \tag{1}$$

where ψ_j, $j = 1, 2, \ldots, n$ are n complex scalar macroscopic wavefunctions. We focus here on the Manakov system of repulsive interactions $g_{ij} = 1$ for simplicity, but the numerical setup is not limited to this constraint. Indeed, both the linear limit continuation and the driving-induced dynamics are not limited to Manakov interactions in any particular way. Interestingly, even the SU(n)-induced dynamics may persist for many breathing cycles when the SU(n) symmetry is only approximately satisfied [20,21,61]. While earlier spinor condensates [25,32] also contain spin-dependent interactions [35,63], recently spinor condensates with Manakov interactions became available [33]. Moreover, the work is also partially motivated by multicomponent nonlinear optical problems [64]. Nevertheless, we expect that the solitary waves considered herein should be relevant more broadly, as spin-dependent interactions are typically quite small, and solitary waves frequently exist in a much broader setting than the specific parameters at which they are solved. We discuss deviations from the Manakov limit in the Supplemental Material, demonstrating the robustness of the methods and the results presented herein [65].

The condensates, unless otherwise specified, are confined in a harmonic trap of the form

$$V = \tfrac{1}{2}x^2, \tag{2}$$

where the trapping frequency is set to 1 by scaling without loss of generality [61]. Stationary states of the form

$$\psi_j(x,t) = \psi_j^0(x)e^{-i\mu_j t} \tag{3}$$

lead to n coupled stationary equations:

$$-\frac{1}{2}\psi_{jxx}^0 + V\psi_j^0 + \left(\sum_{k=1}^{n} g_{jk}|\psi_k^0|^2\right)\psi_j^0 = \mu_j\psi_j^0, \tag{4}$$

where μ_j is the chemical potential of the jth component. To connect the model to experiments, we briefly summarize the transformations leading to Eq. (1) and the units used in this work, and we refer the interested readers to [61] for further details. First, the GPE in physical units is reduced in dimension from three to an effective one dimension by integrating out the frozen y, z ground states. Next, the one-dimensional (1D) equation is made dimensionless using the regular harmonic oscillator scaling in quantum mechanics [66]. After these steps, the effective trap frequency is 1 and the effective interaction strength is $g_{\rm 1D} = \frac{2\omega_\perp a_s}{\omega_x \ell_x}$, and a final simple scaling in the wavefunctions by $(g_{\rm 1D})^{1/2}$ changes the effective interaction strength to $g_{ij} = 1$ as well. Here, a_s, ω_x, $\omega_\perp$, $\ell_x = (\hbar/(m\omega_x))^{1/2}$ stand for the s-wave scattering length, the axial and transverse trapping frequencies, and the axial harmonic oscillator length in physical units, respectively. In summary, our length is measured in units of ℓ_x, time in units of $1/\omega_x$, and the chemical potential in units of $\hbar\omega_x$. The number of particles in the jth component is $N_j = \frac{1}{g_{\rm 1D}}\int |\psi_j|^2 dx$. The prefactor in the atom numbers arises purely from the final mathematical scaling of the wavefunctions setting effectively $g_{ij} = 1$.

Equation (1) has n U(1) symmetries; i.e., if $(\psi_1, \ldots, \psi_n)^T$ is a solution, then $(\psi_1 e^{i\theta_1}, \ldots, \psi_n e^{i\theta_n})^T$ is also a solution, where $\{\theta_j\}$ are real numbers. In the Manakov case, there is an additional SU(n) symmetry. It is straightforward to show that

$$(\psi_1', \ldots, \psi_n')^T = U(\psi_1, \ldots, \psi_n)^T \tag{5}$$

is also a solution if U is unitary, $UU^\dagger = \mathbb{I}$. Note that the total density profile is invariant upon the rotation, i.e., $\sum_j |\psi_j'|^2 = \sum_j |\psi_j|^2$. Because a stationary state typically has a different chemical potential for each component, the state after rotation is typically a dynamical one. In order to illustrate this rotation more clearly, we here provide a concrete example. Consider a two-component stationary solution [Eq. (3)]; then

$$\psi_1'(x,t) = \left(\psi_1^0(x)e^{-i\mu_1 t} + \psi_2^0(x)e^{-i\mu_2 t}\right)/\sqrt{2}, \tag{6}$$

$$\psi_2'(x,t) = \left(\psi_1^0(x)e^{-i\mu_1 t} - \psi_2^0(x)e^{-i\mu_2 t}\right)/\sqrt{2}, \tag{7}$$

is also a solution for the specific unitary matrix:

$$U = \frac{1}{\sqrt{2}}\begin{pmatrix} 1 & 1 \\ 1 & -1 \end{pmatrix}. \tag{8}$$

When $\mu_1 \neq \mu_2$, the rotated waves will become dynamical ones. However, the total density profile remains stationary and identical to that of the stationary state before rotation.

Our numerical simulations for each solitary wave include identifying a series of stationary states following a continuation path in the chemical potential parameter space, computing the BdG stability spectrum along the path, and finally conducting dynamics of the solitary waves. The numerical details are summarized in the Appendix for clarity, and we turn to the linear limit continuation in the next section.

B. Construct vector solitary waves from the linear limit

The idea of constructing solitary waves from the linear limit is extremely simple but effective. For completeness, we start from the one-component setting. In this case, each harmonic oscillator state $|n_1\rangle$ with the chemical potential or eigenvalue $n_1 + 1/2$ can be continued to the Thomas-Fermi regime containing n_1 dark solitons [58]. In this process, the number of particles, N, is approximately zero near the linear limit, and then it grows as the chemical potential is increased. For example, the ground state has a linear limit at $\mu_1 = 0.5$ as a faint Gaussian function. As the chemical potential increases, it becomes the Thomas-Fermi ground state. The first excited state has a linear limit at $\mu_1 = 1.5$, and in a similar process it turns into a single dark soliton state embedded in the Thomas-Fermi sea. The nonlinear wave stemming from the linear state $|n_1\rangle$ contains a total of n_1 dark solitons, which can be conveniently labeled as $\mathcal{S}_{n_1}$. Here, $\mathcal{S}$ stands for a state or soliton.

TABLE I. Number of states with distinct quantum numbers from the linear limit. There are a total of $C_{n_1}^{n-1} = \frac{n_1!}{(n-1)!(n_1-n+1)!}$ states in the family n_1 (the maximum quantum number) for the n-component system. Note that the asymptotic growth speed is increasingly rapid as the number of components, n, grows.

n	$n_1 = 0$	1	2	3	4	5	6	7	8	9	10
1	1	1	1	1	1	1	1	1	1	1	1
2		1	2	3	4	5	6	7	8	9	10
3			1	3	6	10	15	21	28	36	45
4				1	4	10	20	35	56	84	120
5					1	5	15	35	70	126	210

For a two-component system, the linear limit has two quantum numbers from the two independent harmonic oscillators $|n_1, n_2\rangle$ [59,61]. The state has its linear limit at $(\mu_1, \mu_2) = (n_1 + 1/2, n_2 + 1/2)$. We focus here on states $n_1 > n_2 \geqslant 0$, as it is not hard to prove that $\langle \psi_i^0 | \psi_j^0 \rangle (\mu_i - \mu_j) = 0$; i.e., if two states are not orthogonal, they must have the same chemical potential. For example, the state $|1, 1\rangle$ can indeed be continued to the stationary dark-dark soliton, but because the two components must have the same chemical potential, the two profiles are in fact identical up to a scaling factor. This state is therefore somewhat trivial in the sense that it can be obtained by splitting the corresponding single dark soliton state of the one-component system. Note that if ψ^0 is a one-component stationary state, then $(c_1\psi^0, c_2\psi^0)^T$ is a stationary state of the two-component Manakov system if $|c_1|^2 + |c_2|^2 = 1$. Such splitting can be readily generalized: if we have an n-component stationary state, we can split any of the components in the same way to get an $(n+1)$-component stationary state. Therefore, we focus here on irreducible states where all the pertinent quantum numbers are distinct. The two-component system was recently systematically explored in [61]. The low-lying states are $\mathcal{S}_{10}$, $\mathcal{S}_{20}$, and $\mathcal{S}_{21}$ corresponding to the well-known single dark-bright, the in-phase two dark-bright, and the out-of-phase two dark-bright structures, respectively.

The procedure can be readily generalized to n-component systems. Specifically, we can continue the harmonic oscillator state $|n_1, \dots, n_n\rangle$ to the solitary wave $\mathcal{S}_{n_1,\dots,n_n}$, where again $n_1 > \cdots > n_n \geqslant 0$. In this work, we explore the three-component setting systematically, and further study some prototypical low-lying states in four- and five-component systems. It should be noted that the number of states grows very rapidly with the increasing principle quantum number n_1 in multicomponent systems. It is straightforward to show that the number of states in the family n_1 for the n-component system is given by $C_{n_1}^{n-1} = \frac{n_1!}{(n-1)!(n_1-n+1)!} \sim \frac{n_1^{n-1}}{(n-1)!}$ as $n_1 \to \infty$. The asymptotic growth rate with n_1 is therefore increasingly rapid as n increases: it is constant for $n = 1$, linear for $n = 2$, quadratic for $n = 3$, and so on. The numbers of low-lying states are summarized in Table I. In this work, we exhaust all the states in the three-component system up to $n_1 = 4$, and study some typical higher-lying states up to $n_1 = 10$. In four- and five-component systems, we study the respective six lowest-lying states. We see below that these state profiles are already quite complex.

III. NUMERICAL RESULTS

A. Vector solitary waves from the linear limit

We start from the three-component system. The first few low-lying states $\mathcal{S}_{210}$, $\mathcal{S}_{310}$, $\mathcal{S}_{320}$, $\mathcal{S}_{321}$, and their BdG spectra are depicted in Fig. 1. All the solitary waves studied herein are also illustrated in yet larger sizes in the Supplemental material for better clarity [65]. The first observation is that these states exist, and all of them contain certain unstable modes (the red curves of the spectra are for the real part of the eigenvalues λ_r and instabilities; the blue curves are for the imaginary part of the eigenvalues λ_i and stable modes). By contrast, the one-component dark soliton and the two-component dark-bright soliton and even the in-phase two dark-bright solitons appear to be very robust structures [61]. Similarly, the stability tends to be improved as a state moves towards the Thomas-Fermi limit, and there are suitable chemical potential intervals where these solitary waves are fully stable. It should be noted that the instabilities are very weak though for these low-lying structures; the real part of the eigenvalues is enlarged by a factor of 10 in Fig. 1 for ease of visualization, i.e., the maximum growth rate is only about $0.3/10 = 0.03$ (cf. the dimensionless trapping frequency 1).

In order to gain more insight on the structures, we examine the total density profile (as an effective density potential) and the density profiles of the trapping first component and the trapped second and third components, shown in the bottom panels of Fig. 1. The phase part is not plotted because the stationary wavefunctions here are real valued, and the wavefunction of any component changes sign whenever it crosses a node or a dark soliton. Interestingly, the total density profiles are quite different among the structures; they also do not exhibit a Thomas-Fermi structure, but local density minimums are found in all cases, in line with [67]. In state $\mathcal{S}_{210}$, there is a double-well potential structure; the two peaks of the second component concentrate at the two wells while the third component is trapped at the center by the edges of the double well. Note that each component is also trapped by the external harmonic potential. The state $\mathcal{S}_{310}$ has three density wells: the two peaks of the second component occupy the side wells while the peak of the third component concentrates in the central well. The state $\mathcal{S}_{320}$ also has three wells, but the side ones are deeper. Here, the second component has three peaks that sit in the three wells; the central peak is the most prominent. The third component has two prominent peaks concentrated in the two side wells. It also has a finite weight with a barely peak structure in the central well. The state $\mathcal{S}_{321}$ has a single funnel-like potential trapping altogether both the second and third components with three and two peaks, respectively. These five peaks of the two components are organized alternatively, with the side peaks larger and the central peaks smaller.

Next, there are a total of six states in the family $n_1 = 4$, $\mathcal{S}_{410}$, $\mathcal{S}_{420}$, $\mathcal{S}_{421}$, $\mathcal{S}_{430}$, $\mathcal{S}_{431}$, and $\mathcal{S}_{432}$, as illustrated in Fig. 2. The former two states are relatively robust, while the latter four states are more prone to instabilities. Nevertheless, all of these states can be suitably stabilized. Similarly, the total density profile (not shown) again varies among the structures, and local density minimums are found and they are correlated with the density peaks of the trapped second and third components.

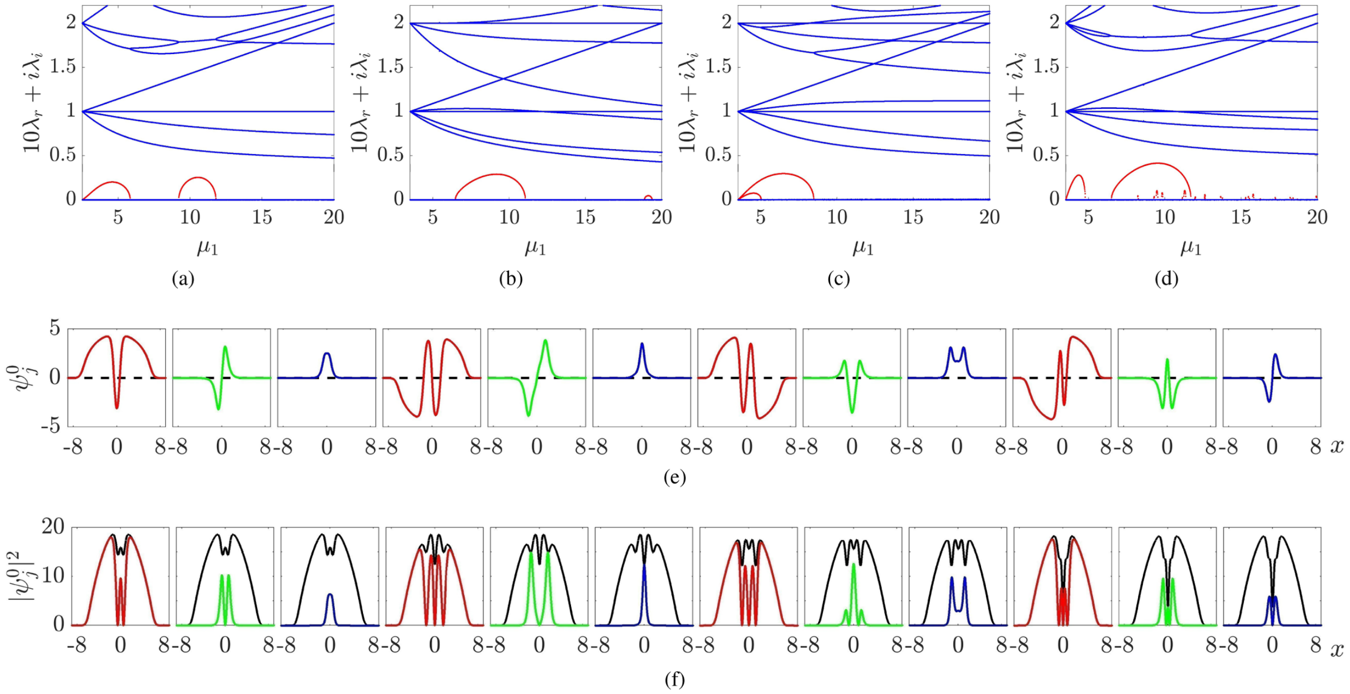

FIG. 1. Top: The BdG spectra λ of the states $\mathcal{S}_{210}$, $\mathcal{S}_{310}$, $\mathcal{S}_{320}$, and $\mathcal{S}_{321}$, respectively, along a linear trajectory from the respective linear limits $(n_1 + 0.5, n_2 + 0.5, n_3 + 0.5)$ to a typical large-density limit (20,18,16) in the (μ_1, μ_2, μ_3) parameter space. Red (the low-lying bubbles) and blue points are for the (unstable) real and (stable) imaginary parts of the eigenvalues, respectively. These states all feature wide ranges of spectral stability in chemical potentials. Middle: Typical configurations at $\mu_1 = 20$ are depicted for the respective states above, and the three components are in turn plotted in red, green, and blue. A larger version is also shown in the Supplemental Material [65]. Bottom: The total density profile (black line) and the density profiles of each component are depicted, suggesting that the total density provides an effective trapping potential and the density peaks of different components tend to avoid each other due to the intercomponent repulsions.

It is clearly impossible to exhaust all of the states, and we turn to representative ones in the following. We emphasize that this is only due to the large number of states available, and in this work we have not encountered any linear state that cannot be continued to its corresponding nonlinear counterpart. It seems that for a given n_1 the lowest-lying structure, i.e., $\mathcal{S}_{n_1 10}$, has the best stability, in agreement with the two-component setting [61]. In the following, we therefore focus on such states for simplicity up to $n_1 = 10$. In addition, we also consider the state $\mathcal{S}_{531}$ which contains a central dark-dark-dark structure; this is the lowest-lying state where all the quantum numbers are odd. These states are summarized in Figs. 3 and 4. These states too can be fully stabilized, and we do not repeatedly mention this fact every time as this is true for *all* the structures we studied.

We can readily identify the well-known building blocks of the localized dark-dark-dark, dark-dark-bright, and dark-bright-bright structures [32,53] in the obtained states. The central part of $\mathcal{S}_{531}$ is a dark-dark-dark soliton, while the other two structures are rather common. For example, the central part of $\mathcal{S}_{210}$ is a dark-bright-bright soliton and the central part of $\mathcal{S}_{310}$ is a dark-dark-bright soliton, and such structures are also prevalent off the center. It is perhaps even more interesting that the decomposition of a solitary wave into an array of localized structures is, however, frequently not relevant, contrary to one- and two-component structures. One striking example is the state $\mathcal{S}_{1010}$: the third component is highly localized and the "lattice" is consequently rather heterogeneous. The second component fills the density dips of the dark soliton lattice at the sides while the third component fills the density dips around the center; the third component essentially disappears at the sides of the lattice, rendering the sides effectively two-component dark-bright lattices.

As the states get increasingly complex, they also become harder to stabilize, which appears to be a generic feature [61]. There are more unstable modes and the growth rates are also larger. The state $\mathcal{S}_{1010}$ becomes relatively robust only when $\mu_1 \gtrsim 50$. As the number of components grows, the spectrum is also more sensitive to the particular choice of the final chemical potentials or the continuation path, compared with one- and two-component systems. We find that a structure tends to be more readily stabilized if the peak densities, which are correlated with the respective chemical potentials, do not vary significantly between adjacent components.

Finally, the linear limit continuation can be readily applied to four- and five-component systems, despite that the induced solitary waves inevitably become increasingly complex in their structures, and their numbers also grow much more rapidly (see Table I). Here, we only present the six lowest-lying states for each setting in Figs. 5 and 6, respectively. While none of these structures is fully robust in general, which is not surprising as this is already the case for three components, it is nevertheless remarkable that all of them again can be fully stabilized in suitable chemical potential intervals.

It is clearly beyond the scope of this work to explore the detailed properties of the (large array of) solitary waves continued from the linear limit, which are important in their own rights. Future work can focus on their structures with

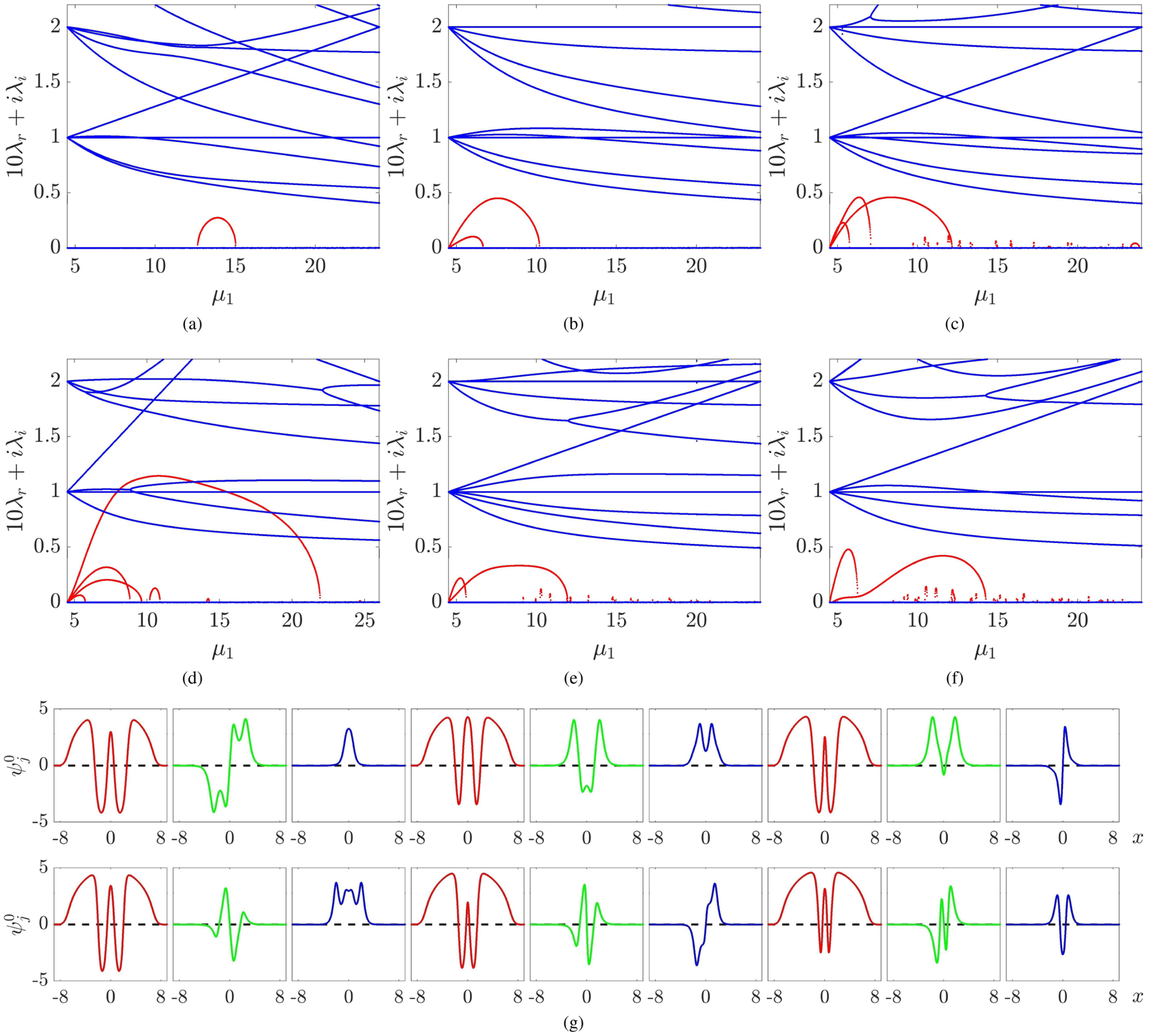

FIG. 2. Same as Fig. 1 but for the $n_1 = 4$ family of states $\mathcal{S}_{410}$, $\mathcal{S}_{420}$, $\mathcal{S}_{421}$, $\mathcal{S}_{430}$, $\mathcal{S}_{431}$, and $\mathcal{S}_{432}$, respectively. The final chemical potentials are (24,22,20), except for the $\mathcal{S}_{430}$ state. The state does not become fully stable along this trajectory, but can be stabilized when we extend it further into the Thomas-Fermi regime. Here, its final chemical potentials are only slightly larger (26,22,20).

particle picture descriptions, e.g., using the variational method [58]. Their modes of instabilities and symmetry-breaking bifurcations are also interesting to explore. Next, we turn to their diverse dynamics.

B. SU(n)-induced and driving-induced dynamics

Numerous dynamical scenarios are expected [30], and here we present only a few proof-of-principle dynamics of these solitary waves. We focus on two types as mentioned previously: one is the SU(n)-induced beating dynamics [20,61,67] and the other is driving-induced dynamics [28]. Both lead to oscillatory dark solitons, but they have quite different features and mechanisms. For the driving-induced dynamics, we apply a constant force to the "bright solitons," i.e., to the component stemming from the $|0\rangle$ state. For the SU(n)-induced dynamics, we use for simplicity the following symmetric SU(2) (for a subrotation) and SU(n) rotations:

$$U_{2\times 2} = \frac{1}{\sqrt{2}}\begin{pmatrix} 1 & 1 \\ 1 & -1 \end{pmatrix}, \tag{9}$$

$$U_{3\times 3} = \frac{1}{\sqrt{3}}\begin{pmatrix} 1 & 1 & 1 \\ 1 & w_1 & w_2 \\ 1 & w_2 & w_1 \end{pmatrix}, \tag{10}$$

$$U_{4\times 4} = \frac{1}{2}\begin{pmatrix} 1 & 1 & 1 & 1 \\ 1 & 1 & -1 & -1 \\ 1 & -1 & 1 & -1 \\ 1 & -1 & -1 & 1 \end{pmatrix}, \tag{11}$$

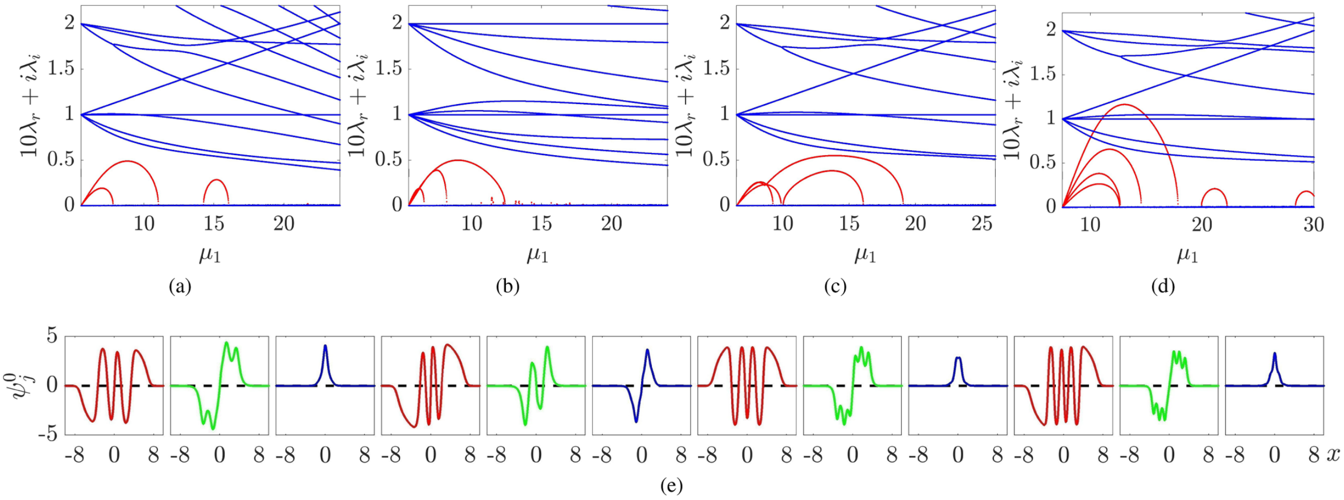

FIG. 3. Same as Fig. 1 but for a few higher-lying states $\mathcal{S}_{510}$, $\mathcal{S}_{531}$, $\mathcal{S}_{610}$, and $\mathcal{S}_{710}$, with final chemical potentials (24,22,20), (24,22,20), (26,22,20), and (30,24,22), respectively. Note that the state $\mathcal{S}_{531}$ has all odd quantum numbers, and the center is a dark-dark-dark structure.

$$U_{5\times5} = \frac{1}{\sqrt{5}}\begin{pmatrix} 1 & 1 & 1 & 1 & 1 \\ 1 & z_1 & z_2 & z_3 & z_4 \\ 1 & z_2 & z_4 & z_1 & z_3 \\ 1 & z_3 & z_1 & z_4 & z_2 \\ 1 & z_4 & z_3 & z_2 & z_1 \end{pmatrix}, \tag{12}$$

where $w_k = \exp(i2k\pi/3)$, $k = 1$, 2, and $z_k = \exp(i2k\pi/5)$, $k = 1, 2, 3, 4$. While these matrices are clearly specific, it is worth mentioning that any SU(n) matrix works and they may likely produce yet more breathing patterns.

We first illustrate both types of dynamics for the $\mathcal{S}_{210}$ state; the results are summarized in Fig. 7. The first panel illustrates an SU(3)-induced beating pattern, and each component contains two dark solitons. This dynamics is coincidentally periodic as the chemical potentials here satisfy $\mu_1 - \mu_2 = \mu_2 - \mu_3$. In more general settings the dynamics would not be periodic, such as the SU(3) beating pattern of the $\mathcal{S}_{310}$ state shown below, which at least has a much longer period. The second panel shows a subspace SU(2)-induced beating pattern mixing the first and the third components, producing the out-of-phase two dark-dark beating pattern. It is interesting that the second component sits exactly still while the other two components are very dynamical. This is as expected because the SU(n) rotation does not change the total density profile. More generally, for a subspace SU(n) rotation, the unrotated components will similarly remain stationary. The third panel shows a driving-induced oscillation. Here, we apply a

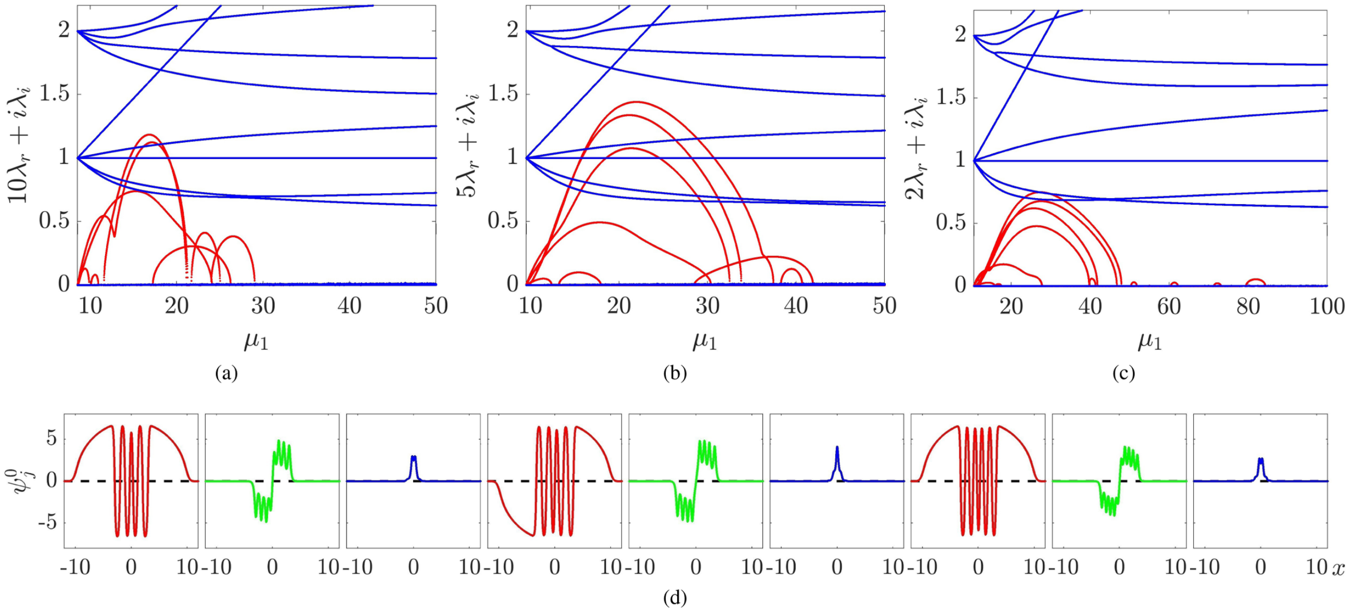

FIG. 4. Same as Fig. 1 but for three highly excited states $\mathcal{S}_{810}$, $\mathcal{S}_{910}$, and $\mathcal{S}_{1010}$, with final chemical potentials (50,36,32), (50,36,32), and (100,70,64), respectively. Here, the depicted configurations are at $\mu_1 = 50$ instead. Note the different scaling factors for the real part of the eigenvalues. It is interesting that the third component is mostly concentrated in the center, while the second component fills the off-center density dips of the dark soliton lattice, rendering the "lattice" rather heterogeneous.

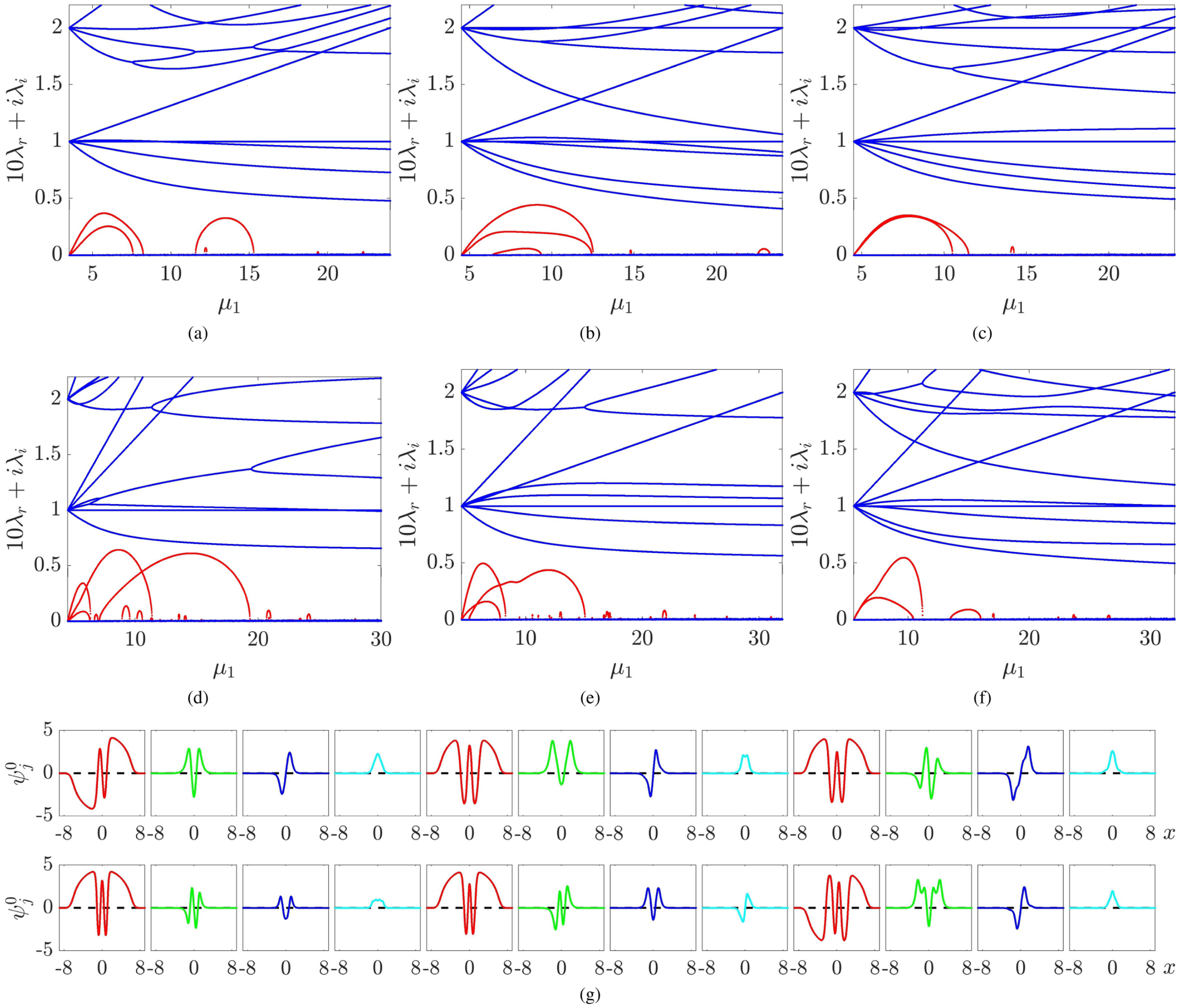

(a) (b) (c) (d) (e) (f) (g)

FIG. 5. The first six low-lying four-component states $\mathcal{S}_{3210}$, $\mathcal{S}_{4210}$, $\mathcal{S}_{4310}$, $\mathcal{S}_{4320}$, $\mathcal{S}_{4321}$, and $\mathcal{S}_{5210}$ with final chemical potentials (24,22,20,18), (24,22,20,18), (24,22,20,18), (30,24,20,16), (32,28,26,22), and (32,28,26,22), respectively. The depicted states are at $\mu_1 = 20$, and the fourth component is shown in cyan.

force $F = 0.1$ to the third component along the negative x axis. Note that this component is somewhat locally trapped by the dark soliton of the second component. This is like a dark-bright structure (focusing on the latter two components); upon driving, due to the negative mass of the dark soliton, the central soliton propagates against the driving potential. It then decelerates, stopped by the driving potential, and then reverses its motion and finally closes a cycle. This is similar to the two-component dark-bright AC oscillation in [28] but with simple Manakov interactions in our setting. Here, the dynamics is more complicated due to the presence of the first component. The two dark solitons therein are also slightly excited (e.g., its out-of-phase oscillation mode). The bright component dynamics is slightly "rugged" as it is influenced by the central mass of the first component (note that this is particularly the case when the bright soliton oscillates back to the trap center). Nevertheless, the prominent oscillation in the latter two components is pretty robust, and the solitary wave structures are well preserved.

The second row shows the same dynamics but for the $\mathcal{S}_{310}$ state. The SU(3)-induced beating pattern has three dark solitons in each component, and, as mentioned above, the dynamics is no longer periodic (or at least has a much longer period) upon a close inspection. The subspace SU(2) rotation is applied to the second and third components, producing a simple dark-dark beating pattern. Similarly, the first component stands completely still while the other two components undergo dynamics. The driving-induced AC oscillation is much cleaner, and all the components are genuinely and coherently excited compared with that of $\mathcal{S}_{210}$. This is because the central structure is a dark-dark-bright structure rather than a dark-bright-bright structure as in the $\mathcal{S}_{210}$ state. It is easier to

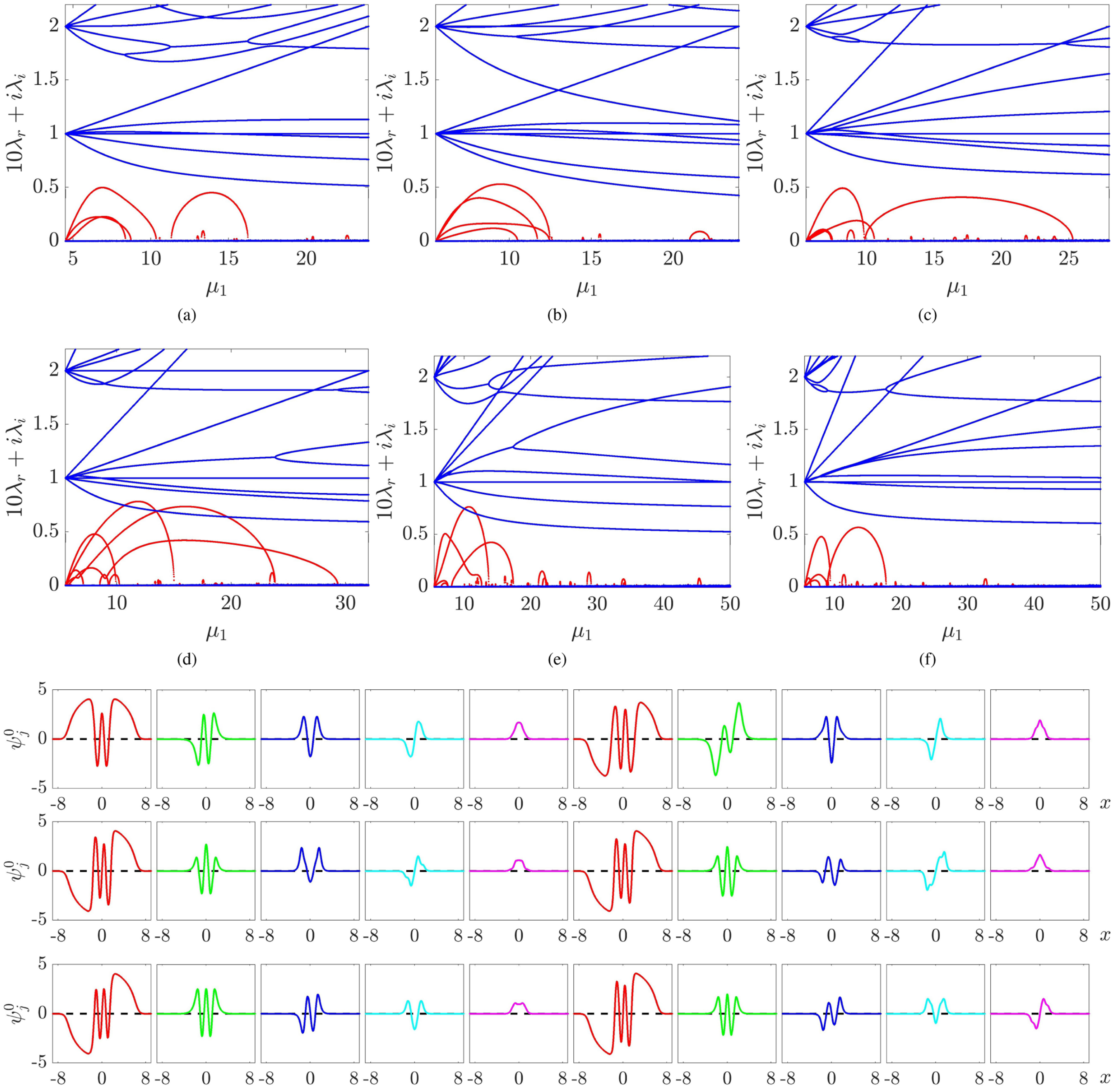

FIG. 6. The first six low-lying five-component states $\mathcal{S}_{43210}$, $\mathcal{S}_{53210}$, $\mathcal{S}_{54210}$, $\mathcal{S}_{54310}$, $\mathcal{S}_{54320}$, and $\mathcal{S}_{54321}$ with final chemical potentials (24,22,20,18,16), (24,22,20,18,16), (28,24,20,18,16), (32,28,24,22,20), (50,46,41,36,30), and (50,42,38,36,34), respectively. The depicted states are at $\mu_1 = 20$, and the fifth component is shown in pink.

balance when two dark solitons are trapping a bright soliton than when one dark soliton traps two bright solitons when one bright soliton is driven.

The third row is for the $\mathcal{S}_{1010}$ state. In the SU(3)-induced beating pattern, there are ten dark solitons in each component. Interestingly, the central breathing dynamics differs from that of the sides. This is also reflected in the subspace SU(2)-rotation-induced dynamics in Fig. 7(h) where the central dark solitons breathe while the side ones are essentially stationary in the first and third components. These are clearly consequences of the heterogeneous structure of the $\mathcal{S}_{1010}$ state itself. The final panel, Fig. 7(i), shows the driving-induced AC oscillation. The dynamics is more complex as there are multiple dark and bright solitons involved, e.g., the two bright peaks are clearly not symmetric (note that the peak density on the right is much higher). Nevertheless, the oscillation remains robust despite that the structure is much more complex.

Next, two examples are illustrated for each SU(4)- and SU(5)-induced beating dynamics in Fig. 8. These patterns are pretty complicated, and the dark soliton velocities are highly asynchronized; i.e., they do not reach their minimum or maximum speeds simultaneously. Note that these patterns

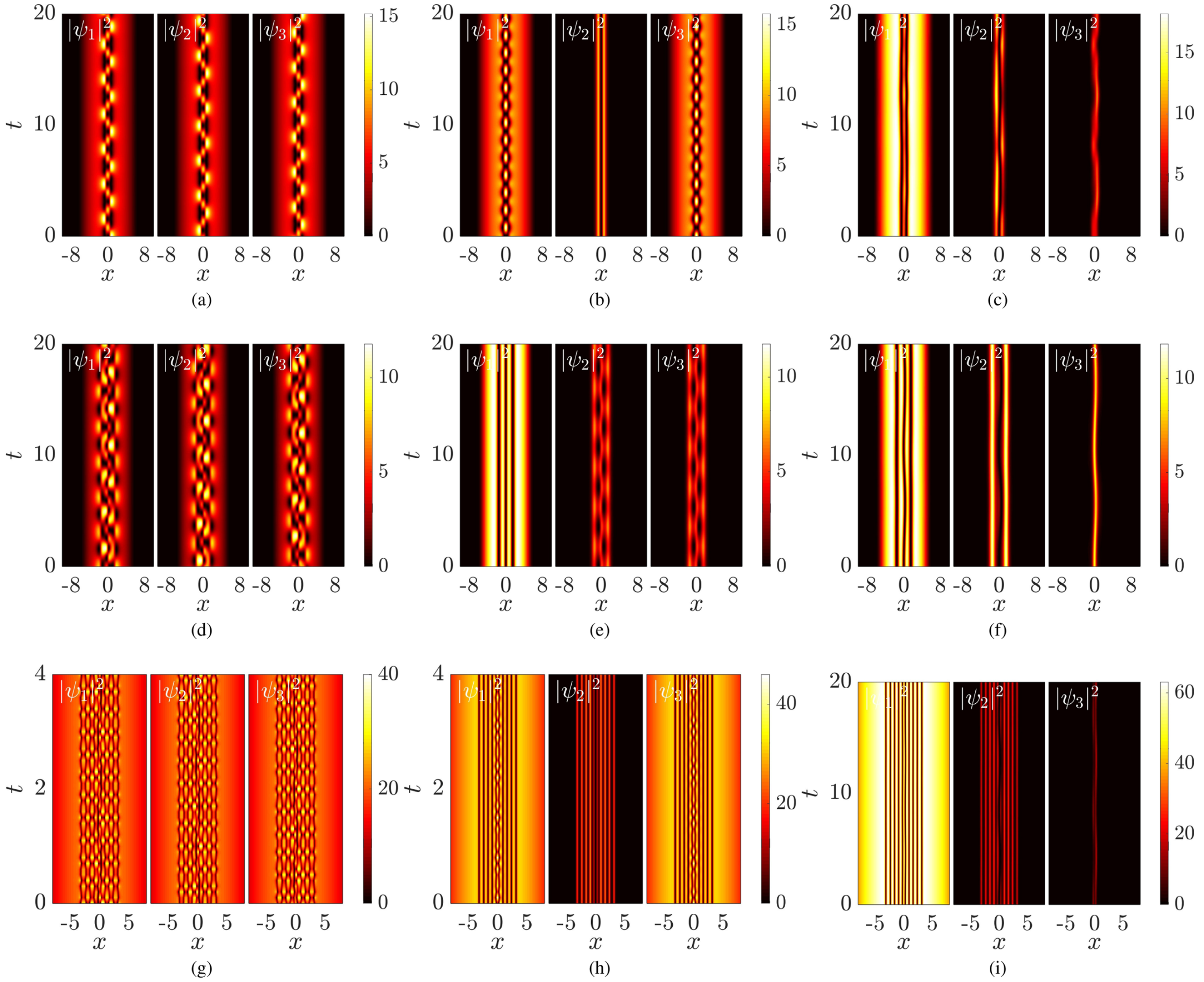

FIG. 7. Top: SU(3)-induced dark soliton beating patterns: (a) For the state $\mathcal{S}_{210}$ at $\mu_1 = 20$, each component contains two dark solitons due to the intercomponent mixing. (b) An SU(2)-induced out-of-phase dark-dark beating pattern; here, the first and the third components are mixed. (c) We apply a driving force along the negative x axis to the third component, producing the dark-bright AC oscillation in the second and third components; note that the first component is also excited. Middle: The same but for the $\mathcal{S}_{310}$ state at $\mu_1 = 16$. Here, there are three solitons in each component in (d), and the SU(2) rotation mixes the second and the third components. In (f), all components are excited in the AC oscillation, as the central structure is a dark-dark-bright soliton. Bottom: The same but for the $\mathcal{S}_{1010}$ state at $\mu_1 = 70$. Interestingly, the rotated dynamics are also quite heterogeneous. For example, in (h) the first and third components are mixed: the central dark solitons undergo beating dynamics while the side ones are essentially stationary.

are already obtained from very symmetric rotations; if the rotation was less symmetric, the patterns would become even more complicated. Here, the beating patterns again can be either periodic or aperiodic depending on the specific chemical potentials. It is also possible to study subspace rotations and driving-induced dynamics and so on, and we do not investigate these further here.

Finally, we discuss promising experimental implementations of these solitary waves and their dynamics, considering the tremendous control presently available in manipulating cold atoms. Reference [41] illustrates that it is possible to controllably produce dark solitary waves of arbitrary speed in a single-component condensate using both density and phase engineering [41–43]. Vector solitary waves can then be generated in multicomponent systems using the techniques recently pinioned in [33], where a spatially localized spin rotation with simultaneous density and phase imprinting can be achieved with a steerable laser beam. It is worth mentioning that while we have constructed the waves using the chemical potential continuation, experimentalists can directly implement a profile in a stable regime. Additionally, the SU(n)-induced dynamics can be initialized either directly or alternatively one can first prepare a stationary state and then mix the components using Rabi oscillations [68]. The driving force to one component can be implemented using a Stern-Gerlach inhomogeneous magnetic field, e.g., when the atoms are in hyperfine states $|20\rangle$, $|10\rangle$, and $|11\rangle$ in an optically trapped three-component condensate.

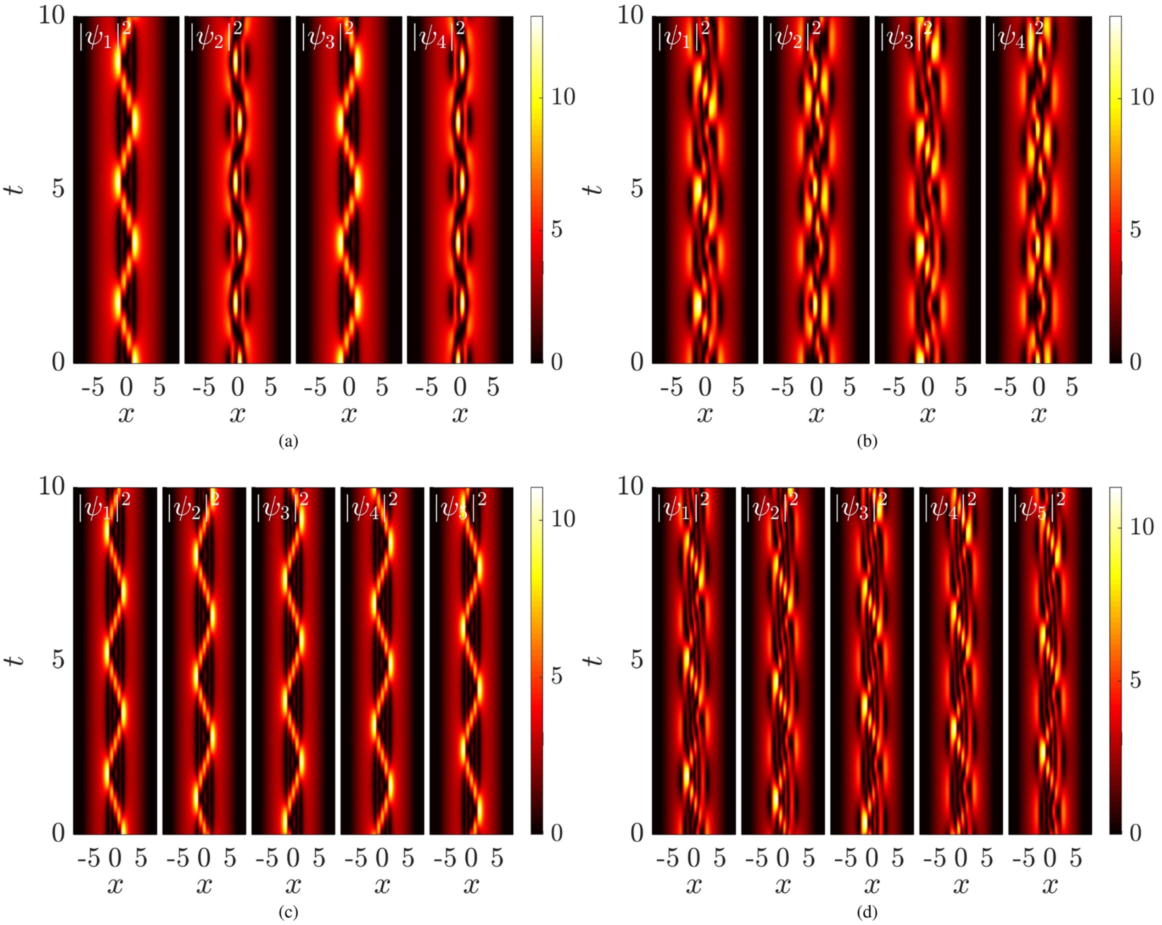

(a) (b) (c) (d)

FIG. 8. Top: SU(4)-induced beating patterns for the states (a) $\mathcal{S}_{3210}$ and (b) $\mathcal{S}_{4210}$ at $\mu_1 = 20$; each component contains three and four dark solitons, respectively, due to the intercomponent mixing. Bottom: SU(5)-induced beating patterns for the states (c) $\mathcal{S}_{43210}$ and (d) $\mathcal{S}_{53210}$ at $\mu_1 = 20$; each component contains four and five dark solitons, respectively. The (a) and (c) dynamics are periodic due to the special chemical potentials; the (b) and (d) dynamics at least have much longer periods.

IV. CONCLUSIONS AND FUTURE CHALLENGES

In this work, we presented a systematic construction of stationary vector solitary waves from their linear limits in three-, four-, and five-component Bose-Einstein condensates with repulsive Manakov interactions. We reveal their waveforms and also find suitable chemical potential intervals where they can be fully stabilized. Their waveforms are much more complex than the one- and two-component counterparts. For example, a solitary wave typically cannot be decomposed as a collection of elementary vector solitons, and there are also interesting emerging structures like a heterogeneous lattice. The number of waves also scales much faster with respect to the principle quantum number n_1 as the number of components n increases, asymptotically as $\frac{n_1^{n-1}}{(n-1)!}$. Some SU(n)-induced and driving-induced dynamics producing dark soliton oscillation patterns are also illustrated. These robust and rich structures and their versatile dynamics are ideal for future theoretical investigation and experimental implementation.

Our work also demonstrates the effectiveness of the method of constructing solitary waves from the linear limit. The work can be extended in various directions, even in the present one-dimensional setting. First, studying cases away from the Manakov limit is interesting; one can look for, e.g., dark-antidark states [22]. Second, it is also interesting to study the cases where the masses of the different components are distinct. Here, a component with a smaller quantum number may trap a component with a larger quantum number depending on the mass ratios [69]. Third, it is highly interesting to include also the spin-dependent interactions.

Another interesting research track is to continue from the integrable analytical limit [49–52]. Here, asymmetric stationary states are available. If a state settles to constants in the ±∞ limits, we can gradually turn on a strong but finite box potential to render the condensates finite, and then continue the state further to the harmonic trap using, e.g., an interpolation in the potentials. It should be noted that parametric continuation can start from any analytically tractable limit; there is no reason the linear limit should be the starting point. Our preliminary results suggest this is possible. This is significant in that it makes a bridge between the integrable limit and the trapped settings. Future work should examine whether this may generate asymmetric waves in the harmonic potential.

The work should be naturally extended to higher dimensions, where the method is much more versatile because of the emergence of degenerate states at the linear limit and the additional freedom of asymmetric traps. It should be noted that there has already been a number of such studies on particular states, including quite "complicated" multiple vortex ring structures in three dimensions [70]. Here, our focus is different. The question is not how to construct a particular state based on physical insight, but rather to look for well-defined rules to construct solitary waves again systematically, regardless what solitary waves come out. Obviously, each linear state is a good candidate for continuation. Next, mixing degenerate states may produce novel solitonic structures; this is very different from the one-dimensional setting as bound states therein cannot degenerate. For example, in a two-dimensional symmetric trap, states $|n_x n_y\rangle = |10\rangle$ and $|01\rangle$ are degenerate; each produces a dark soliton stripe state. By contrast, the $(|10\rangle \pm i|01\rangle)/\sqrt{2}$ linear states produce a single vortex [7] and antivortex state of unit charge, respectively. Similarly, the linear state $(|20\rangle + |02\rangle)/\sqrt{2}$ yields a dark soliton ring and so on, demonstrating the diversity of the possibilities.

The first step is to find all possible sets of degenerate states; this can be readily solved and can even be visualized using the lattice planes of the quantum number "lattice." The nontrivial part is how to mix a set of degenerate states. Proper rules should be articulated such that one can efficiently generate as many distinct solitary waves as possible yet following a simple procedure. One possibility is that for any set of degenerate states of size k, we can choose any $m \leqslant k$ states out of the set and mix them using different coefficients, e.g., $\pm 1, \pm i$. If a distinct state is found, it should be continued and also added to the degenerate set. More sophisticated rules or numerical refinements should be considered, and we do not discuss this further here. Our preliminary results on the one-component two-dimensional system suggest that this conceptually straightforward strategy of continuation from the linear limit systematically appears to be very powerful and no less efficient than the current state-of-the-art methods [55–57] with its own distinct features, and it is capable of producing a (very) large array of solitary waves ahead. Research work along these lines is currently in progress, and will be reported in future publications.

ACKNOWLEDGMENTS

We thank P. G. Kevrekidis and Lichen Zhao for helpful discussions. We gratefully acknowledge support from the National Science Foundation of China under Grant No. 12004268, the Fundamental Research Funds for the Central Universities, China, and the Science Speciality Program of Sichuan University under Grant No. 2020SCUNL210. We thank the Emei cluster at Sichuan University for providing HPC resources.

APPENDIX: NUMERICAL DETAILS AND THE BDG ANALYSIS

In this Appendix, we present the numerical details, including the BdG stability analysis of the n-component GPE. A stationary state, given a proper initial guess as detailed below, is computed using a finite element method for the discretization of space and the iterative Newton method towards convergence. The linear oscillator states are used as the initial guess for a stationary state near but not at the linear limit, and the converged state is then served as the initial guess for the next nearby chemical potentials and so on. We use a linear "trajectory" for simplicity in the multidimensional $\vec{\mu} = (\mu_1, \ldots, \mu_n)^T$ parameter space; i.e., given the linear limit chemical potentials $\vec{\mu}_i$ and the final (chosen) chemical potentials $\vec{\mu}_f$, the trajectory is given by $\vec{\mu} = \vec{\mu}_i + \epsilon(\vec{\mu}_f - \vec{\mu}_i)$, where $\epsilon \in (0, 1]$ is a parameter interpolating the two points. If $\vec{\mu}_i$ and $\vec{\mu}_f$ are given, it is sufficient to specify a point by either ϵ or any of the chemical potentials, e.g., μ_1 as we do in this work. To find the first weakly coupled stationary state, we set the initial chemical potentials approximately $O(0.01)$ away from the linear limit. The final point is empirically chosen such that the maximum densities do not vary significantly between adjacent components, while keeping the order of the chemical potentials unchanged; i.e., we keep $\mu_1 > \cdots > \mu_n$. In fact, the continuation of states is pretty robust and straightforward in the one-dimensional setting; the careful selection of the final chemical potentials is to help find spectrally stable states.

The BdG stability spectrum is computed for each stationary state along the trajectory. The BdG analysis is a linear stability analysis of a stationary state, and we now calculate the BdG matrix. First, we introduce the following perturbation *Ansätze* around the stationary states of Eq. (3):

$$\psi_j(x,t) = e^{-i\mu_j t}\left\{\psi_j^0(x) + \varepsilon\left(a_j(x)e^{\lambda t} + b_j^*(x)e^{\lambda^* t}\right)\right\}, \quad \text{(A1)}$$

where $\varepsilon \ll 1$. Upon substituting Eq. (A1) into the GPE of Eq. (1), we obtain at order $O(\varepsilon)$ an eigenvalue problem of the form

$$Mv = \lambda v, \quad \text{(A2)}$$

where $v = (a_1, b_1, \ldots, a_n, b_n)^T$ and the matrix M is given by the following compact form:

$$M = \Lambda[D + \bar{G}\cdot(\bar{\psi}\bar{\psi}^\dagger)], \quad \text{(A3)}$$

where

$$\Lambda = \mathrm{diag}[-i, i, \ldots, -i, i], \quad \text{(A4)}$$

$$D = \mathrm{diag}[\mathcal{L}_1 + U_1, \mathcal{L}_1 + U_1, \ldots, \mathcal{L}_j + U_j, \mathcal{L}_j + U_j, \ldots], \quad \text{(A5)}$$

$$\mathcal{L}_j = -\frac{1}{2}\frac{\partial^2}{\partial x^2} + V - \mu_j, \quad \text{(A6)}$$

$$U_j = \sum_k g_{jk}\left|\psi_k^0\right|^2, \quad \text{(A7)}$$

$$\bar{G} = \mathrm{kron}(G, \mathrm{ones}(2,2)), \quad G_{ij} = g_{ij}, \quad \text{(A8)}$$

$$\bar{\psi} = \left(\psi_1^0, \psi_1^{0*}, \ldots, \psi_n^0, \psi_n^{0*}\right)^T. \quad \text{(A9)}$$

Here, $C = A\cdot B$ denotes the element-by-element multiplication, i.e., $C_{ij} = A_{ij}B_{ij}$; ones(2, 2) is a 2×2 matrix with all elements equal to 1; and the kron(A, B) operator expands the A matrix, where each element A_{ij} is replaced by the block matrix $A_{ij}B$. One can readily check that when $n = 3$, the matrix correctly restores the BdG matrix of the three-component GPE [61].

For each stationary state, we compute the first 100 low-lying eigenvalues in magnitude and the eigenvectors, which correspond to the low-lying excitation modes. The eigenvalues are generally complex: $\lambda = \lambda_r + i\lambda_i$. If there are modes with $\lambda_r > 0$, the state is dynamically unstable with respect to perturbations. On the other hand, if all the eigenvalues are entirely imaginary, the state is robust and dynamically stable. As the states get more excited, i.e., containing more dark soliton phase windings, the number of unstable modes stemming from the linear limit tends to increase, which requires higher chemical potentials to suppress the instabilities. This consequently requires both a larger domain (due to a larger Thomas-Fermi radius) and a finer spacing (due to a smaller healing length) for a fixed prescribed accuracy; i.e., it gets increasingly expensive to fully stabilize more excited states.

We select spectrally stable states at suitable chemical potentials for SU(n)-induced [20] and driving-induced [28] dynamics. For the former dynamics, different components are mixed [according to Eq. (5) at, e.g., $t = 0$] producing (a)periodic beating patterns depending on the specific chemical potentials. It is worth emphasizing that the rotation operation itself is not described by the GPE, and is applied only once, after which the rotated fields continue the evolution according to the GPE again. Indeed, the respective norms are typically changed by the rotation operation. Experimentally, one can either directly imprint the after-rotation field profiles or alternatively start from a stationary state and then mix components with spin-interconversion Rabi oscillations [68]. For the driving dynamics, we suddenly turn on at $t = 0$ a constant driving force $F > 0$ along the negative x axis to one component; i.e., the component experiences an additional linear potential of $V_D = Fx$. This can be implemented experimentally using an inhomogeneous magnetic field (see Sec. III for more discussions). In this work, we drive the "bright" component which has no node, producing approximately periodic orbits [28]. Our dynamics are integrated using the regular fourth-order Runge-Kutta method.

[1] L. Pitaevskii and S. Stringari, *Bose-Einstein Condensation* (Oxford University Press, Oxford, UK, 2003).

[2] C. Pethick and H. Smith, *Bose-Einstein Condensation in Dilute Gases* (Cambridge University Press, Cambridge, UK, 2002).

[3] Y. S. Kivshar and B. Luther-Davies, Dark optical solitons: Physics and applications, Phys. Rep. **298**, 81 (1998).

[4] P. G. Kevrekidis, D. J. Frantzeskakis, and R. Carretero-González, *The Defocusing Nonlinear Schrödinger Equation: From Dark Solitons to Vortices and Vortex Rings* (SIAM, Philadelphia, 2015).

[5] F. Abdullaev, A. Gammal, A. Kamchatnov, and L. Tomio, Dynamics of bright matter wave solitons in a Bose-Einstein condensate, Int. J. Mod. Phys. B **19**, 3415 (2005).

[6] D. J. Frantzeskakis, Dark solitons in atomic Bose-Einstein condensates: From theory to experiments, J. Phys. A: Math. Theor. **43**, 213001 (2010).

[7] A. L. Fetter and A. A. Svidzinsky, Vortices in a trapped dilute Bose-Einstein condensate, J. Phys.: Condens. Matter **13**, R135 (2001).

[8] A. L. Fetter, Rotating trapped Bose-Einstein condensates, Rev. Mod. Phys. **81**, 647 (2009).

[9] S. Komineas, Vortex rings and solitary waves in trapped Bose-Einstein condensates, Eur. Phys. J.: Spec. Top. **147**, 133 (2007).

[10] D. Proment, M. Onorato, and C. F. Barenghi, Vortex knots in a Bose-Einstein condensate, Phys. Rev. E **85**, 036306 (2012).

[11] G. Theocharis, D. J. Frantzeskakis, P. G. Kevrekidis, B. A. Malomed, and Y. S. Kivshar, Ring Dark Solitons and Vortex Necklaces in Bose-Einstein Condensates, Phys. Rev. Lett. **90**, 120403 (2003).

[12] W. Wang, P. G. Kevrekidis, and E. Babaev, Ring dark solitons in three-dimensional Bose-Einstein condensates, Phys. Rev. A **100**, 053621 (2019).

[13] T. Busch and J. R. Anglin, Dark-Bright Solitons in Inhomogeneous Bose-Einstein Condensates, Phys. Rev. Lett. **87**, 010401 (2001).

[14] S. Rajendran, P. Muruganandam, and M. Lakshmanan, Interaction of dark-bright solitons in two-component Bose-Einstein condensates, J. Phys. B: At. Mol. Opt. Phys. **42**, 145307 (2009).

[15] G. Dean, T. Klotz, B. Prinari, and F. Vitale, Dark-dark and dark-bright soliton interactions in the two-component defocusing nonlinear Schrödinger equation, Appl. Anal. **92**, 379 (2013).

[16] C. Hamner, J. J. Chang, P. Engels, and M. A. Hoefer, Generation of Dark-Bright Soliton Trains in Superfluid-Superfluid Counterflow, Phys. Rev. Lett. **106**, 065302 (2011).

[17] D. Yan, J. J. Chang, C. Hamner, P. G. Kevrekidis, P. Engels, V. Achilleos, D. J. Frantzeskakis, R. Carretero-González, and P. Schmelcher, Multiple dark-bright solitons in atomic Bose-Einstein condensates, Phys. Rev. A **84**, 053630 (2011).

[18] E. T. Karamatskos, J. Stockhofe, P. G. Kevrekidis, and P. Schmelcher, Stability and tunneling dynamics of a dark-bright soliton pair in a harmonic trap, Phys. Rev. A **91**, 043637 (2015).

[19] G. C. Katsimiga, P. G. Kevrekidis, B. Prinari, G. Biondini, and P. Schmelcher, Dark-bright soliton pairs: Bifurcations and collisions, Phys. Rev. A **97**, 043623 (2018).

[20] D. Yan, J. J. Chang, C. Hamner, M. Hoefer, P. G. Kevrekidis, P. Engels, V. Achilleos, D. J. Frantzeskakis, and J. Cuevas, Beating dark-dark solitons in Bose-Einstein condensates, J. Phys. B: At. Mol. Opt. Phys. **45**, 115301 (2012).

[21] E. G. Charalampidis, W. Wang, P. G. Kevrekidis, D. J. Frantzeskakis, and J. Cuevas-Maraver, SO(2)-induced breathing patterns in multicomponent Bose-Einstein condensates, Phys. Rev. A **93**, 063623 (2016).

[22] G. C. Katsimiga, S. I. Mistakidis, T. M. Bersano, M. K. H. Ome, S. M. Mossman, K. Mukherjee, P. Schmelcher, P. Engels, and P. G. Kevrekidis, Observation and analysis of multiple dark-antidark solitons in two-component Bose-Einstein condensates, Phys. Rev. A **102**, 023301 (2020).

[23] C. Qu, L. P. Pitaevskii, and S. Stringari, Magnetic Solitons in a Binary Bose-Einstein Condensate, Phys. Rev. Lett. **116**, 160402 (2016).

[24] A. Farolfi, D. Trypogeorgos, C. Mordini, G. Lamporesi, and G. Ferrari, Observation of Magnetic Solitons in Two-Component Bose-Einstein Condensates, Phys. Rev. Lett. **125**, 030401 (2020).

[25] X. Chai, D. Lao, K. Fujimoto, R. Hamazaki, M. Ueda, and C. Raman, Magnetic Solitons in a Spin-1 Bose-Einstein Condensate, Phys. Rev. Lett. **125**, 030402 (2020).

[26] X. Chai, D. Lao, K. Fujimoto, and C. Raman, Magnetic soliton: From two to three components with SO(3) symmetry, Phys. Rev. Res. **3**, L012003 (2021).

[27] X. Chai, L. You, and C. Raman, Magnetic solitons in an immiscible two-component Bose-Einstein condensate, arXiv:2011.11462.

[28] L.-C. Zhao, W. Wang, Q. Tang, Z.-Y. Yang, W.-L. Yang, and J. Liu, Spin soliton with a negative-positive mass transition, Phys. Rev. A **101**, 043621 (2020).

[29] L.-C. Zhao and J. Liu, Rogue-wave solutions of a three-component coupled nonlinear Schrödinger equation, Phys. Rev. E **87**, 013201 (2013).

[30] P. G. Kevrekidis and D. J. Frantzeskakis, Solitons in coupled nonlinear Schrödinger models: A survey of recent developments, Rev. Phys. **1**, 140 (2016).

[31] Y. V. Kartashov, V. A. Vysloukh, L. Torner, and B. A. Malomed, Self-trapping and splitting of bright vector solitons under inhomogeneous defocusing nonlinearities, Opt. Lett. **36**, 4587 (2011).

[32] T. M. Bersano, V. Gokhroo, M. A. Khamehchi, J. D'Ambroise, D. J. Frantzeskakis, P. Engels, and P. G. Kevrekidis, Three-Component Soliton States in Spinor $F = 1$ Bose-Einstein Condensates, Phys. Rev. Lett. **120**, 063202 (2018).

[33] S. Lannig, C.-M. Schmied, M. Prüfer, P. Kunkel, R. Strohmaier, H. Strobel, T. Gasenzer, P. G. Kevrekidis, and M. K. Oberthaler, Collisions of Three-Component Vector Solitons in Bose-Einstein Condensates, Phys. Rev. Lett. **125**, 170401 (2020).

[34] S. V. Manakov, On the theory of two-dimensional stationary self-focusing of electromagnetic waves, Sov. J. Exp. Theor. Phys. **38**, 248 (1974).

[35] Y. Kawaguchi and M. Ueda, Spinor Bose-Einstein condensates, Phys. Rep. **520**, 253 (2012).

[36] C. Becker, S. Stellmer, P. Soltan-Panahi, S. Dörscher, M. Baumert, E.-M. Richter, J. Kronjäger, K. Bongs, and K. Sengstock, Oscillations and interactions of dark and dark-bright solitons in Bose-Einstein condensates, Nat. Phys. **4**, 496 (2008).

[37] S. Stellmer, C. Becker, P. Soltan-Panahi, E.-M. Richter, S. Dörscher, M. Baumert, J. Kronjäger, K. Bongs, and K. Sengstock, Collisions of Dark Solitons in Elongated Bose-Einstein Condensates, Phys. Rev. Lett. **101**, 120406 (2008).

[38] L. M. Aycock, H. M. Hurst, D. K. Efimkin, D. Genkina, H.-I. Lu, V. M. Galitski, and I. B. Spielman, Brownian motion of solitons in a Bose-Einstein condensate, Proc. Natl. Acad. Sci. U.S.A. **114**, 2503 (2017).

[39] A. Weller, J. P. Ronzheimer, C. Gross, J. Esteve, M. K. Oberthaler, D. J. Frantzeskakis, G. Theocharis, and P. G. Kevrekidis, Experimental Observation of Oscillating and Interacting Matter Wave Dark Solitons, Phys. Rev. Lett. **101**, 130401 (2008).

[40] G. Theocharis, A. Weller, J. P. Ronzheimer, C. Gross, M. K. Oberthaler, P. G. Kevrekidis, and D. J. Frantzeskakis, Multiple atomic dark solitons in cigar-shaped Bose-Einstein condensates, Phys. Rev. A **81**, 063604 (2010).

[41] A. R. Fritsch, M. Lu, G. H. Reid, A. M. Piñeiro, and I. B. Spielman, Creating solitons with controllable and near-zero velocity in Bose-Einstein condensates, Phys. Rev. A **101**, 053629 (2020).

[42] J. E. Williams and M. J. Holland, Preparing topological states of a Bose-Einstein condensate, Nature (London) **401**, 568 (1999).

[43] L. D. Carr, J. Brand, S. Burger, and A. Sanpera, Dark-soliton creation in Bose-Einstein condensates, Phys. Rev. A **63**, 051601(R) (2001).

[44] M.-S. Chang, C. D. Hamley, M. D. Barrett, J. A. Sauer, K. M. Fortier, W. Zhang, L. You, and M. S. Chapman, Observation of Spinor Dynamics in Optically Trapped ^{87}Rb Bose-Einstein Condensates, Phys. Rev. Lett. **92**, 140403 (2004).

[45] M.-S. Chang, Q. Qin, W. Zhang, L. You, and M. S. Chapman, Coherent spinor dynamics in a spin-1 Bose condensate, Nat. Phys. **1**, 111 (2005).

[46] J. Stenger, S. Inouye, D. M. Stamper-Kurn, H.-J. Miesner, A. P. Chikkatur, and W. Ketterle, Spin domains in ground-state Bose-Einstein condensates, Nature (London) **396**, 345 (1998).

[47] H.-J. Miesner, D. M. Stamper-Kurn, J. Stenger, S. Inouye, A. P. Chikkatur, and W. Ketterle, Observation of Metastable States in Spinor Bose-Einstein Condensates, Phys. Rev. Lett. **82**, 2228 (1999).

[48] H. Schmaljohann, M. Erhard, J. Kronjäger, M. Kottke, S. van Staa, L. Cacciapuoti, J. J. Arlt, K. Bongs, and K. Sengstock, Dynamics of $F = 2$ Spinor Bose-Einstein Condensates, Phys. Rev. Lett. **92**, 040402 (2004).

[49] V. B. Matveev and M. A. Salle, *Darboux Transformation and Solitons* (Springer-Verlag, Berlin, 1991).

[50] E. V. Doktorov and S. B. Leble, *A Dressing Method in Mathematical Physics* (Springer-Verlag, Berlin, 2007).

[51] R. Hirota, *The Direct Method in Soliton Theory* (Cambridge University Press, Cambridge, UK, 2004).

[52] T. Kanna and M. Lakshmanan, Exact Soliton Solutions, Shape Changing Collisions, and Partially Coherent Solitons in Coupled Nonlinear Schrödinger Equations, Phys. Rev. Lett. **86**, 5043 (2001).

[53] L. Ling, L.-C. Zhao, and B. Guo, Darboux transformation and multi-dark soliton for N-component nonlinear Schrödinger equations, Nonlinearity **28**, 3243 (2015).

[54] In addition to numerically exact solutions, there are also approximate analytical solutions by using, e.g., perturbation theory near the linear limit or variational method in the opposite Thomas-Fermi regime.

[55] E. G. Charalampidis, P. G. Kevrekidis, and P. E. Farrell, Computing stationary solutions of the two-dimensional Gross-Pitaevskii equation with deflated continuation, Commun. Nonlinear Sci. Numer. Simul. **54**, 482 (2018).

[56] E. G. Charalampidis, N. Boullé, P. E. Farrell, and P. G. Kevrekidis, Bifurcation analysis of stationary solutions of two-dimensional coupled Gross-Pitaevskii equations using deflated continuation, Commun. Nonlinear Sci. Numer. Simul. **87**, 105255 (2020).

[57] N. Boullé, E. G. Charalampidis, P. E. Farrell, and P. G. Kevrekidis, Deflation-based identification of nonlinear excitations of the three-dimensional Gross-Pitaevskii equation, Phys. Rev. A **102**, 053307 (2020).

[58] M. P. Coles, D. E. Pelinovsky, and P. G. Kevrekidis, Excited states in the large density limit: A variational approach, Nonlinearity **23**, 1753 (2010).

[59] W. Wang and P. G. Kevrekidis, Transitions from order to disorder in multiple dark and multiple dark-bright soliton atomic clouds, Phys. Rev. E **91**, 032905 (2015).

[60] W. Wang and P. G. Kevrekidis, Two-component dark-bright solitons in three-dimensional atomic Bose-Einstein condensates, Phys. Rev. E **95**, 032201 (2017).

[61] W. Wang, L.-C. Zhao, E. G. Charalampidis, and P. G. Kevrekidis, Dark-dark soliton breathing patterns in multi-component Bose-Einstein condensates, J. Phys. B: At. Mol. Opt. Phys. **54**, 055301 (2021).

[62] B. Xiong and J. Gong, Dynamical creation of complex vector solitons in spinor Bose-Einstein condensates, Phys. Rev. A **81**, 033618 (2010).

[63] D. M. Stamper-Kurn and M. Ueda, Spinor Bose gases: Symmetries, magnetism, and quantum dynamics, Rev. Mod. Phys. **85**, 1191 (2013).

[64] Q-Han Park and H. J. Shin, Systematic construction of multicomponent optical solitons, Phys. Rev. E **61**, 3093 (2000).

[65] See Supplemental Material at http://link.aps.org/supplemental/10.1103/PhysRevE.104.014217 for further results beyond the Manakov limit, and also stationary state configurations in yet larger sizes.

[66] C. Cohen-Tannoudji, B. Diu, and F. Laloë, *Quantum Mechanics* (Wiley, New York, 1977), translation of *Mécanique quantique* (Hermann, Paris, 1973).

[67] L.-C. Zhao, Beating effects of vector solitons in Bose-Einstein condensates, Phys. Rev. E **97**, 062201 (2018).

[68] H. E. Nistazakis, Z. Rapti, D. J. Frantzeskakis, P. G. Kevrekidis, P. Sodano, and A. Trombettoni, Rabi switch of condensate wave functions in a multicomponent Bose gas, Phys. Rev. A **78**, 023635 (2008).

[69] E. G. Charalampidis, P. G. Kevrekidis, D. J. Frantzeskakis, and B. A. Malomed, Dark-bright solitons in coupled nonlinear Schrödinger equations with unequal dispersion coefficients, Phys. Rev. E **91**, 012924 (2015).

[70] W. Wang, R. N. Bisset, C. Ticknor, R. Carretero-González, D. J. Frantzeskakis, L. A. Collins, and P. G. Kevrekidis, Single and multiple vortex rings in three-dimensional Bose-Einstein condensates: Existence, stability, and dynamics, Phys. Rev. A **95**, 043638 (2017).